Optical, Mathematical, and Computational Foundations of Lensless Ultra-Miniature Diffractive Imagers and Sensors

David G. Stork and Patrick R. Gill
Computational Sensing and Imaging
Rambus Labs
1050 Enterprise Way, Suite 700
Sunnyvale, CA 94089 USA
{dstork,pgill}@rambus.com

***Abstract*—We describe the optical, mathematical and computational foundations for a new class of lensless, ultra-miniature computational imagers and image sensors. Such sensors employ phase gratings that have provably optimal optical properties and are integrated with CMOS photodetector matrices. These imagers have no lens and can thus be made extremely small ($\sim$100 μm) and very inexpensive (a few Euro cents). Because the apertures are small, they have an effective depth of field ranging from roughly 1 mm to infinity. The grating acts as a two-dimensional visual "chirp" and preserves image power throughout the Fourier plane; thus the captured signals preserve image information. The final digital image is not captured as in a traditional camera but is instead computed from raw photodetector signals. The novel representation at the photodetectors demands powerful algorithms such as deconvolution, Bayesian estimation, or matrix inversion with Tikhonov regularization be used to compute the image, each having different bandwidth, space and computational complexities for a given image fidelity. Such imaging architectures can also be tailored to extract application-specific information or compute decisions (rather than compute an image) based on the optical signal. In most cases, both the phase grating and the signal processing can incorporate prior information about the visual field and the imaging or estimation task at hand. Our sensor design methodology relies on modular parallel and computationally efficient software tools for simulating optical diffraction, for CAD design and layout of gratings themselves, and for sensor signal processing. These sensors are so small they should find use in endoscopy, medical sensing, machine inspection, surveillance and the Internet of Things, and are so inexpensive that they should find use in distributed network applications and in a number of single-use or disposable applications, for instance in military, hazardous natural and industrial conditions.**

Keywords: ***Computational sensing, phase grating, diffractive imager, application-specific sensing, face detection, QR code reading***

I. INTRODUCTION

Recent theoretical and computational advances provide a foundation for a new class of computational optical image sensor: one that forgoes the use of traditional optical elements such as lenses and curved mirrors and relies instead upon diffractive optical elements [1], [2]. Whereas diffractive methods have been employed in other wavebands, such as millimeter-wave imaging, prior, traditional optical imaging architectures have generally been based on the *camera obscura* model—in which each point in the scene is imaged onto a single point on a sensor or image plane. This model has dominated the science and technology of imaging systems for several millennia, at least for sources illuminated by incoherent light. The Chinese philosopher Mo Ti traced an inverted image produced by a pinhole camera to record an image in the fifth century B.C.E. [3] and Johannes Kepler traced a real image projected by a converging lens onto paper in 1603. Chemical recording of projected images, such as by mercury or silver halide, was invented in 1826 and the first true digital camera was built in 1975 [4], all these exploiting the fundamental camera obscura architecture.

As photodetector sensor technology has improved and pixel pitches have become smaller, pixels can be made smaller than the optical diffraction limit of systems such as commercial cameras [5]–[7]. Pixels smaller than the diffraction limit, however, do not provide new image information. Instead, such sub-diffraction-limit pixels provide opportunities to make "smart pixels" with functionality beyond mere direct conversion of photons to electric current [8].

The rise in digital imaging, where image processing can be incorporated into the data chain, has enabled new imaging architectures. Although related concepts were explored in computational radar and x-ray astronomy, it was Cathey and Dowski who took an early and conceptually important step away from the traditional camera obscura model for optical imaging by exploiting digital processing in a deep way [9]. They designed a cubic-phase optical plate which, when inserted into the optical path of a traditional camera, led to an image whose (significant) blur was independent of the object depth: the image on the sensor plane did not "look good" as it would in a traditional camera obscura. Subsequent image processing sharpened the *entire* blurred image, thus leading to enhanced depth of field. Since then the field of *computational imaging* has explored imaging architectures in which the raw signals do not superficially resemble a traditional image; instead, the final image is computed from such signals. More and more of the total imaging "burden" is borne by computation, thereby expanding the class of usable optical components. In this way, many optical aberrations can be corrected computationally rather than optically. This imaging paradigm has led to new conceptual foundations of joint design of optics and image processing [10], as well

as a wide range of non-standard imaging architectures such as plenoptic, coded-aperture and multi-aperture systems, each with associated methods of signal processing [11]–[15].

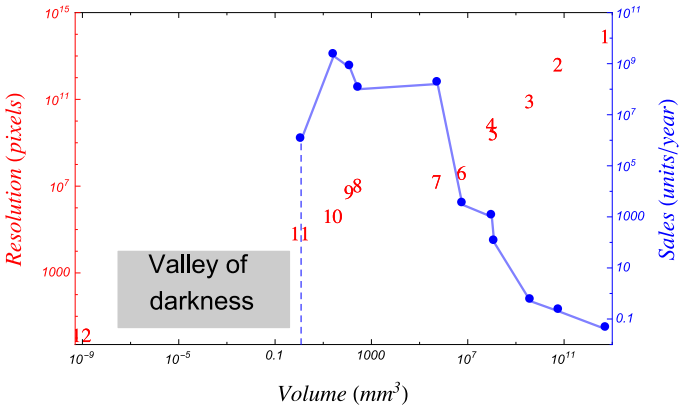

Fig. 1. The left ordinate axis in red shows the resolution (in pixels) versus the physical volume (in mm^3) of representative lens- and mirror-based telescopes and cameras (log-log scale). Notice there is a seven-order-of-magnitude range in physical volume devoid of such cameras (the **Valley of darkness**). 1 Grand Canaria telescope, 2 Hubble telescope, 3 1-m telescope, 4 30-cm telescope, 5 AWARE 2 camera, 6 Professional camera,7 Consumer DSLR, 8 iPhone 5 camera, 9 Pelican camera, 10 Miniature VGA, 11 Medigus camera, 12 Single photodiode (without lens). The right ordinate axis in blue indicates the sales of representative imagers of different physical volumes in units/year worldwide in 2011. (The unit sales figures are estimates based on historical data and market reports and do not include research prototypes and unreleased products.) There is a precipitous drop in sales at the Valley of darkness. Our lensless integrated diffraction grating/CMOS imagers lie within this "valley."

The economic pressures for miniaturization of electronic devices, including cameras, arising in the mobile computing market have led to smaller imager form factors [16]. Figure 1 shows the resolution, in total pixels per exposure, versus physical volume of imaging systems in the traditional camera obscura architecture (or curved mirror equivalent). While such imagers span 22 orders of magnitude in physical volume and 15 orders of magnitude in pixel resolution, the smaller the imager the greater the number sold commercially... but only down to a scale of roughly 1 mm^3. There is a conspicuous gap of seven orders of magnitude in physical volume—the "Valley of darkness"—between the smallest digital camera and a single unlensed photoreceptor. It seems that the camera obscura model has reached its physical limits and cannot be scaled much smaller. A new imaging architecture—with new optical, mathematical and computational foundations—is required to span the Valley of darkness.

Recently, a new miniature imaging architecture has been explored, one based on integrating optics with CMOS photodetectors [2], [17]–[19]. In brief, this architecture forgoes lenses and relies instead on simple square-wave diffraction gratings created in CMOS itself. The earliest designs in this architecture relied on CMOS wires to act as amplitude optical grating patches, the gratings producing a wavelet-like representation of the scene on the sensor matrix. More recently, square-wave *phase* gratings have also been explored [20]. For a given image resolution, such diffractive elements enable the construction of imagers much smaller than does the basic camera obscura model. (We mention in passing that related CMOS structures have been explored for integrated spectroscopy as well [21].) Note too that as given by the trends in resolution versus physical volume evident in Fig. 1, imagers in the Valley of darkness will have nominal resolutions (pixels per single frame) lower than roughly 10^5 pixels [22], [23]. Nevertheless, such low-resolution imagers—or high-resolution sensors—should find use in many applications, especially in the Internet of Things (see Section V).

There are a number of limitations of such previous work. First, amplitude gratings based on CMOS wires have poor low-light sensitivity because most of the incident light never strikes the photodetector. Second, regular diffraction gratings are by their very nature wavelength sensitive, i.e., the pattern of light on the photodetectors depends strongly upon the wavelength of incident light. Third, such imagers are sensitive to manufacturing defects—specifically a small deviation in the thickness of the grating layer can lead to a large (and difficult to correct) alteration of the diffraction pattern on the photodetectors [18].

The method we describe here, while based on integrated silicate phase optics and CMOS image sensors, is fundamentally different from prior work in a number of deep ways. Our method relies on novel special phase anti-symmetric spiral phase gratings, which overcome prior limitations and afford new functionality [24]. Moreover, our new sensor architecture enables the construction of new classes of ultra-miniature sensors whose output is an estimation of some property of the scene (e.g., visual motion) or a decision (e.g., face detection or barcode reading).

We begin in Section II with a discussion of our fundamental technology and turn in Section III to a short description of our software design and analysis tools. We describe our first hardware devices in Section IV. The full results of our hardware verification of the theory and design will be presented at a later date [25]. We mention a few application areas for such sensors and imagers in Section V and conclude in Section VI with some final remarks.

II. Sensor Optics and Technology

The following description of our sensor technology follows the data path—from target source through diffractive optics to photodetector to digital signal processing to final digital image or image estimation.

A. Optics of one-dimensional phase anti-symmetric gratings

The fundamental optical elements employed by our sensors are based on a new type of phase grating having phase antisymmetry. Figure 2 shows a cross section through a UV-curable acrylate binary phase grating, here specified by three free parameters, w_0, w_1 and w_2 [26]. (Generalizations to more free parameters and multiple thicknesses are straightforward.) Consider point **P** lying on the grating's plane of odd symmetry, shown as a vertical dashed red line. The steps in thickness of the acrylate grating correspond to a phase delay of π radians of the typical wavelength used in imaging. Such a phase difference means that light from each position on one side of the plane is cancelled via destructive interference by light from the symmetric position on the other side of the plane

because those waves arrive out of phase. Note especially that such cancellation occurs regardless of the vertical depth of **P**; as such, all points along the red dashed line are dark. We call this plane of destructive interference an "optical curtain" or simply "curtain" [27]. The location of the curtain on the sensor matrix below does not change despite manufacturing errors in overall grating thickness. Finally, as the angle of incidence of the light changes, the curtains tip by the same angle (Fig. 3), a transformation that makes calibration particularly simple problem of estimating a spatial shift. In this way, the sensor responses are invariant to variations in manufactured thickness and wavelength of incident light (Fig. 4). Greater wavelength invariance can be achieved by using an additional layer of silicate with different index of refraction and dispersion coefficient than the primary grating, much as chromatic aberration is corrected in classical lens-based imaging systems through the use of multiple lenses with different indexes of refraction and dispersion [6].

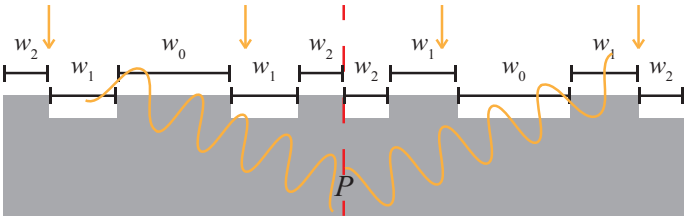

Fig. 2. A cross section through a binary anti-symmetric phase grating, where the plane of odd symmetry is marked with a vertical dashed red line. The parameters w_0, w_1 and w_2 describe the surface profile. For the medium's index of refraction n, the step height is chosen to corresponds to optical phase delay of π radians along the red dashed line or "curtain." For such a phase anti-symmetic grating, curtains exist even if the incident light is not normal.

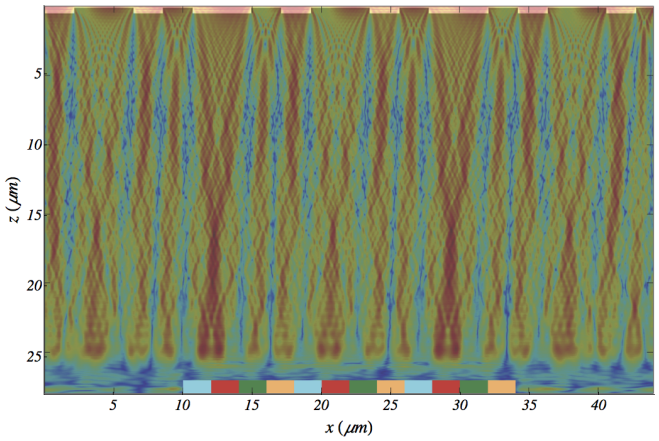

Fig. 3. A finite-difference wave simulation of the electric field energy density for monochromatic light incident at 3.5° passing through a phase anti-symmetric grating where x denotes the position left-to-right and z the depth within the silicate medium. The curtains lie beneath the points of odd symmetry and are tipped at the same angle as the incident light. Such curtains are invariant to the wavelength of incident light. The photodetector matrix, shown as pixels in different colors, lies along the bottom.

B. Phase anti-symmetric spiral gratings

The scenes we seek to image are two-dimensional and therefore the one-dimensional phase anti-symmetric grating and photosensor array just described must be generalized to two dimensions. Specifically, two-dimensional gratings must include segments at every orientation so as to sample the Fourier domain uniformly (and possess no zeros) and thereby enable computational reconstruction of the image from sensor responses. Figure 5 shows two examples of basic spiral grating tiles—having four-fold and six-fold chiral symmetry. These spiral grating tiles are constructed by sweeping one-dimensional phase anti-symmetric gratings perpendicularly along the length of each spiral arm. The phase anti-symmetric gratings are lengthened and made more complicated (use more ws) to cover the full tile area and feasible Fourier domain. Both spiral gratings pass information at all orientations and spatial frequencies up to the Nyquist limit, and can be tiled to cover a full photodetector matrix of arbitrary area (Fig. 6) [24]. In actual sensors, incident light covers an area at least as large as that of a full individual tile element.

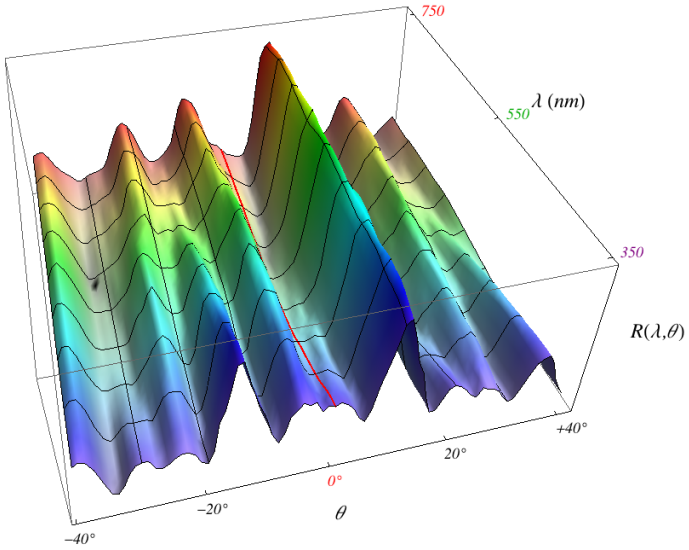

Fig. 4. The response of a single photodetector (pixel) beneath a phase anti-symmetric grating (such as **P** in Fig. 2) as a function of angle of incident light, θ, and wavelength of light, λ. Notice that for normally incident light ($\theta = 0°$) the response nearly vanishes at all wavelengths and that at each incident orientation, the response is nearly invariant with respect to wavelength. The specific form of this response function depends upon the profiles of the grating (described by w_is), which can be tailored to extract information most appropriate to particular applications, including non-imaging applications.

The wave optics described above assumes the incident illumination is plane-wave. In such a case the pattern of light produced by a grating does not depend upon the distance of the object, so long as the object is farther from the sensor than roughly 10 times the spatial scale of the sensor itself. As such, our sensor has extremely large effective depth of field, from roughly 1 mm to infinity.

The pattern of light produced by the diffraction grating strikes the CMOS photodetector matrix beneath and the signals are sent off chip for digital processing.

C. Signal processing

Sensed signals in our sensor do not resemble an image in a camera obscura but must be processed to yield a digital image. We assume the overall forward imaging model is described by:

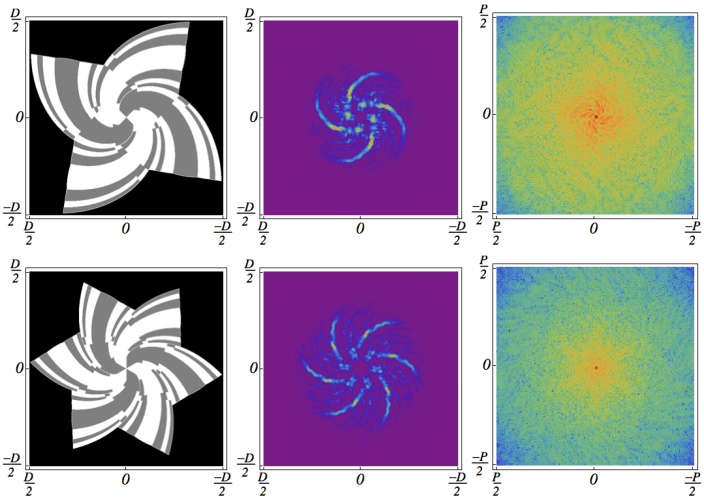

Fig. 5. The left column shows phase anti-symmetric spiral binary gratings, the middle column the point-spread function each produces (both figures of spatial extent $D \times D$, for some distance D). The right column shows the corresponding modulation transfer function (modulus of the Fourier transform) of extent $1/P \times 1/P$, where P is the pixel pitch and determines the Nyquist rate. The top row corresponds to four-fold chiral symmetry and the bottom row corresponds to six-fold chiral symmetry.

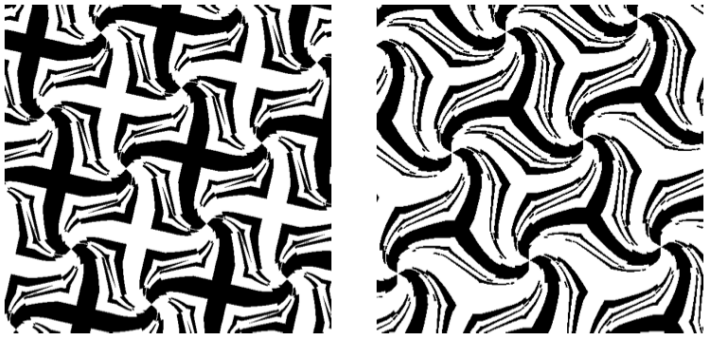

Fig. 6. The individual grating tiles of Fig. 5 can be packed to cover a photodetector matrix of arbitrary area. Alternate approaches to tessellating a sensor array with such individual grating designs are not as space efficient.

$$\mathbf{y} = \mathbf{A}\mathbf{x} + \mathbf{n}, \tag{1}$$

where $\mathbf{y}$ is the vector of photodetector pixel responses, $\mathbf{x}$ is a vector of inputs from the scene, $\mathbf{A}$ the system matrix describing the linear transformation performed by the two-dimensional optical grating, and $\mathbf{n}$ is additive noise, which describes photodetector noise, Poisson photon statistics, quantization noise, etc. (Other models, such as simple multiplicative noise, could also be assumed.) We let $\mathbf{x}$ be m-dimensional, both $\mathbf{y}$ and $\mathbf{n}$ be n-dimensional; hence $\mathbf{A}$ has dimensions $m \times n$.

The regularized least-square estimation problem—that is, the reconstruction of the image—can be expressed as finding the image $\hat{\mathbf{x}}$ that minimizes the error or cost function

$$\mathcal{C} = \|\mathbf{A}\hat{\mathbf{x}} - \mathbf{y}\|^2 + \|\mathbf{\Gamma}\hat{\mathbf{x}}\|^2, \tag{2}$$

where $\mathbf{\Gamma}$ weights the different components of $\hat{\mathbf{x}}$, for instance to accommodate differences prior probabilities of pixel values in the expected scenes. The image that minimizes the cost $\mathcal{C}$ in (2) is [28]

$$\hat{\mathbf{x}} = \left(\mathbf{A}^t\mathbf{A} + \mathbf{\Gamma}^t\mathbf{\Gamma}\right)^{-1}\mathbf{A}^t\mathbf{y}. \tag{3}$$

In the special case that prior information about scene statistics implies that each component of $\hat{\mathbf{x}}$ should be penalized equally ($\mathbf{\Gamma} \propto \mathbf{I}$, the identity matrix), the solution can be written as

$$\hat{\mathbf{x}} = \left(\mathbf{A}^t\mathbf{A} + \gamma\mathbf{I}\right)^{-1}\mathbf{A}^t\mathbf{y}, \tag{4}$$

where γ is a scalar Tikhonov regularization parameter, whose optimal value depends upon the noise level [24], [29]. Cost functions other than that in (2) can be used as well, for instance those based on the *total variation* or *TV* norm of $\hat{\mathbf{x}}$, or on the L_1 norm, or on Bayesian prior information, or on weighted combinations of such penalty terms [30].

The computational burden of estimating the "best" image (in a sum-squared-error sense) compatible with the measured sensor signals $\mathbf{y}$ depends upon the particular form of the cost function $\mathcal{C}$. For the simple Tikhonov regularization in (4), before operation one precomputes the Moore-Penrose pseudo-inverse (possibly for different values of the regularization parameter)—an $\mathcal{O}(n^3)$ operation. Image estimation after signal capture is then a simple matrix multiply, an $\mathcal{O}(n^2)$ operation, easily parallelized to run at video rates in real-time on an FPGA or Graphics Processing Unit, if necessary. We note in passing that under certain circumstances (e.g., the function of the grating can be well approximated by a convolution operation), efficient Fourier estimation methods can be used instead, with an $\mathcal{O}(n \ln n)$ complexity.

Such estimation is well-conditioned and has higher fidelity when the modulation transfer function of the optical element contains no zeros, as is ensured by our spiral anti-symmetry phase gratings. The condition number of the real, non-negative matrix $\mathbf{A}$ is the ratio of the magnitudes of the largest and smallest eigenvalues, i.e.,

$$\kappa(\mathbf{A}) = \frac{|\lambda_{max}|}{|\lambda_{min}|}, \tag{5}$$

which of course is always greater than or equal to 1.0. The smaller the value of $\kappa(\mathbf{A})$, the less noise-prone $\hat{\mathbf{x}}$ will be. For instance, if the matrix is proportional to the identity matrix, that is $\mathbf{A} \propto \mathbf{I}$, then its inverse can be computed with negligible loss in information or in significant bits in its components. Simulation studies of the physics of our phase anti-symmetric spiral gratings show that the condition numbers are roughly 500.

Other reconstruction methods include inverse Wiener filtering and Bayesian methods such as Richardson-Lucy deconvolution [31], each with computational complexities and fidelities that depend upon the accuracy of prior information about the source and other parameters. Figure 7 shows the estimation of an image through simple matrix inversion with Tikhonov regularization summarized in (4).

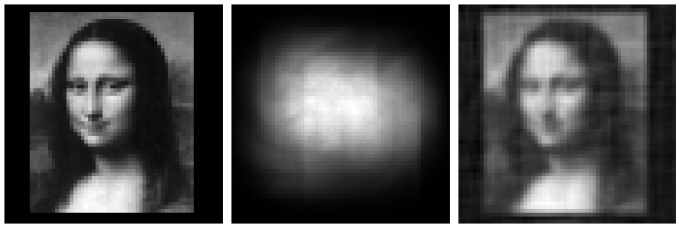

Fig. 7. Image sensing and computational reconstruction of Leonardo's *Mona Lisa* from a lensless phase anti-symmetric spiral phase grating sensor. (Left) The input image. (Middle) The simulated response on the photodetectors due to the six-fold grating in Fig. 5, and (right) the reconstruction by Eq. 4. This image estimate is of higher fidelity than the estimate based on traditional square-wave amplitude gratings and photodetector arrays of comparable number of pixels and overall noise level described in earlier work.

III. Simulation/design tools and methodology

Our sensor system design and analysis methods are based on a modular architecture comprising three software tools, all written in *Matlab* and executed on a large network of PCs:

- **Optics of phase gratings**: We simulate the interaction of light with gratings, for instance by finite-difference wave algorithms. These full-three-dimensional simulations reveal the electromagnetic energy density throughout the silicate grating volume (see Fig. 3) and predict the response of physical photodetector pixels to light of different wavelengths and incident angles, such as in Fig. 4.
- **CAD design of gratings and tiles**: We design gratings (spiral and otherwise) and their tilings starting from a mathematical description of the grating, often parameterized by the number of arms, arm chirality and curvature function, and phase cross-section as a function of distance from the center (i.e., the w_i shown in Fig. 2). The representation of our design is either a *Matlab*-compatible file for wave optics simulations or a *gdsII* file for silicon grating manufacture.
- **Sensor signal processing**: We continue to write our own image reconstruction, signal estimation and pattern recognition software in *Matlab*, often using standard libraries of matrix operations such as Moore-Penrose pseudoinverse. In some research systems, we incorporate free software such as QR code symbol reading software.

We can employ *Perl* software wrappers for these components in order to efficiently design and model the system's end-to-end performance. Such joint design methodology can often lead to superior system performance (higher fidelity reconstruction, few optical elements, etc.) than sequential design, where optics is designed first and only then is the signal processing designed [32].

IV. Hardware implementation

Our experimental hardware implementation of lensless imagers and sensors is based on a single pixel-addressable 10 Mega-pixel sensor from Aptina, Inc., with a single large grating platform comprising 40 experiments (Fig. 8). The gratings are made of a 50-μm-thick layer of acrylic (known as Ugoo)[1] with grating steps of 1.5 μm affixed to a 400-μm-thick glass substrate. Figure 9 shows a micrograph of one portion of the full grating. Input images are presented on an LCD display under computer control, and signals are read directly from the Aptina sensor and processed on a PC.

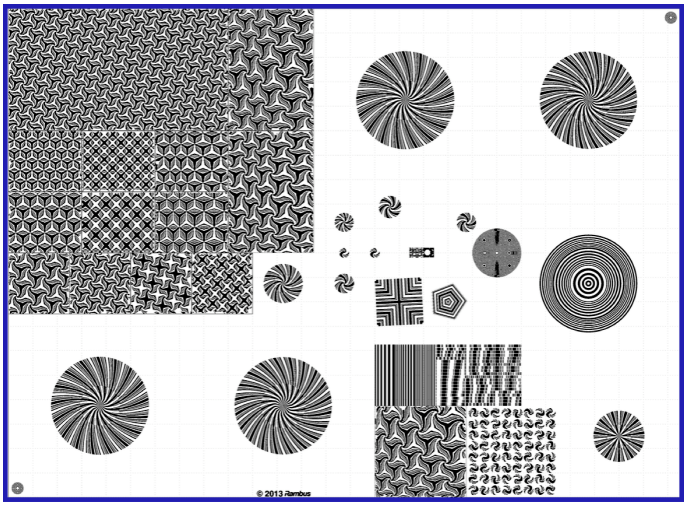

Fig. 8. The Ugoo silicate 5.5×4 mm grating platform contains 40 grating experiments. Some of the experiments involve tesselated areas for applications with lenses, as shown in Fig. 6. Fiducial marks at the lower-left and upper-right of the platform facilitate the estimation of the alignment of the grating with the underlying photodetector matrix.

Physical instantiation of the sensor, calibration of its $\mathbf{A}$ matrix, estimation of noise (photon and circuit), and development of accurate and computationally efficient image reconstruction methods for the hardware as built—all to verify the above theory—is in progress and will be presented separately [25].

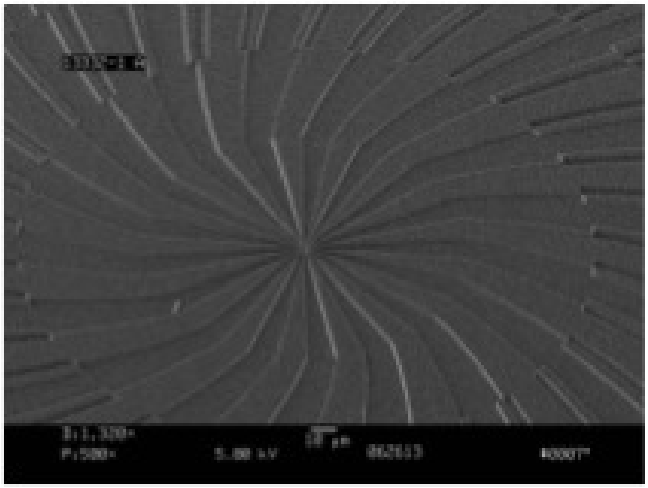

Fig. 9. A scanning electron micrograph of the grating at the lower left in Fig. 8.

V. Applications

There are many promising applications for our computational image sensors, which fall into a number of general

[1] manufactured by Holographix, LLC

categories. It is important to note, though, that these imagers were not designed to compete with high-resolution cameras that are larger and more expensive. Just as most animal and insect vision systems are fairly low resolution but numerous, so too our sensors are designed for numerous applications requiring only relatively simple vision and image analysis. It is as convenient to consider our devices as high-resolution sensors as it is low-resolution imagers.

Some general categories of applications follow.

A. Low-resolution imaging

The ultra-miniature size of our imagers and sensors make them especially appropriate for very small environments in medical and industrial endoscopy as well as traditional and some novel mobile computing devices. There are many surveillance applications that would profit from low- to mid-level resolutions as well. Because these sensors are so inexpensive (in bulk)—each less expensive than a single frame of 35-mm photographic film—they could find application in a number of one-use imaging scenarios arising in military theaters, hazardous industrial conditions (crash tests) and natural environments [32]. Another general area is inexpensive mobile medical imaging and sensing of the form pioneered by Ozcan and his colleagues [33]. A key design decision is where the signal processing should be implemented—close to the sensor itself, or instead on a host machine, possibly delayed from the signal capture.

The sensor described above is panchromatic, that is, it responds to any optical wavelength and yields a monochrome (grayscale) image. There are a number of ways to extend the lensless imaging architecture to yield color images. The most direct method would be to have three separate sensors, each optimized for a different optical wavelength—short, medium and long wavelengths, corresponding to blue, green and red—and integrating the component images.

B. Motion detection and estimation

The optical gratings and signal processing algorithms can be tailored to broad image sensing applications. For instance, because each pixel in such a sensor responds to light from an extended region in the visual field, only a few such pixels need be monitored in order to detect a change in the image. Therefore, such a sensor has very low power dissipation in its waiting or *sentinel* model. Once an image change has occurred, the full complement of pixels can be read so that an image can be captured or motion estimated. This kind of functionality is valuable for occupancy detection for controlled lighting, motion (motion-activated devices), visual looming (pre-impact automotive airbag deployment), interactive toys, and numerous applications in support of the Internet of Things [34].

C. Pattern recognition

These sensors can extract informative visual information for pattern recognition applications, such as face detection (authentication), one-dimensional barcode and two-dimensional QR code reading (Fig. 10), gesture recognition and many others. Of course, the signal processing is then based on principles of pattern recognition appropriate for the task at hand [35], [36]. For instance, QR code symbol reading software must determine the orientation or tip angle of a symbol, and does so by first locating the three fiducial concentric squares visible in Fig. 10 a), c) and d). This first step in QR symbol reading cannot be performed on the raw sensor representation. Moreover, because code analysis and error correction apply to the spatial domain, any lensless diffractive QR code symbol reader should first compute the pixel image of the symbol.

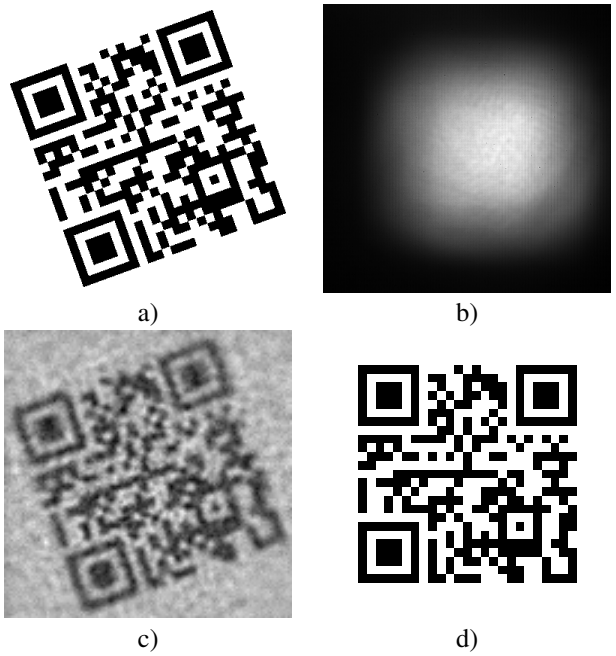

Fig. 10. a) A *Version 2* (25×25) target QR code symbol with information payload of 31 bytes. b) The raw signals in the 400 × 400 pixels array in our computational sensor. c) The digital image computed from the sensor signals using Tikhonov regularization. d) The final digital image, rotated and thresholded by line to yield roughly 50% white pixels. This final image is presented to *ZXing* QR code reading software, which decodes the image to extract its 31-byte code. Note that these barcode images relied on a grating designed for general imaging; a special purpose grating, designed to extract straight lines and right angles, with corresponding digital processing, would likely yield QR symbol images of higher fidelity and higher barcode recognition rates. Note the slight reconstruction errors in the upper-right pixels in d). Despite such slight reconstruction errors, error correction in the symbol reading algorithms ensured this symbol was decoded accurately.

Such a low-resolution sensor is unlikely to support high-accuracy face recognition among many candidate identities [37], but could be used to identify whether some face—*any* face—is present. Such functionality would be valuable for waking up appliances or other connected devices in the Internet of Things. Figure 11 shows the results of realistic simulations of such a face presence detector based on the sensor described above. The classifier is based on a nearest-neighbor algorithm [35, Chapter 4]. The test images consisted of 168 grayscale face images in various orientations and scales as well as simple non-face images. All recognition and classification was performed in the raw sensor representation—no traditional human-interpretable images were computed.

Let $\mathcal{F}$ denote the set of sensor patterns corresponding to faces (including transformations of rotations and scaling), and $\mathcal{G}$ the set of general (i.e., non-face) images. For each of the 168 3600-dimensional patterns $\mathbf{x} \in \mathcal{F}$, we computed the Euclidean distance $D(\mathbf{x}, \mathbf{x}')$ to the nearest other face pattern $\mathbf{x}'$ $(\neq \mathbf{x}) \in \mathcal{F}$. The histogram of such distances is shown at the front of

Fig. 11 in green. Then for each such pattern $\mathbf{x}$ we compute the Euclidean distance to the nearest non-face pattern $\mathbf{x}'' \in \mathcal{G}$. This histogram is shown in red. Of course, on-average such inter-face distances are less than the distances from faces to non-face patterns, i.e., $D(\mathbf{x}, \mathbf{x}') < D(\mathbf{x}, \mathbf{x}'')$. Because there is some overlap in the red and the green histograms, this face detection error is not 0 but in fact roughly 0.09. The Bayes classifier based on this distance D error is shown along the far-right face in Fig. 11.

The above analysis was repeated on the 1800, 900, 400, 200, 100 and 50 features, yielding the additional green and red histograms in Fig. 11. As expected, all histograms shift to smaller overall distance D in the subspaces and the overlap increases; thus the face/non-face error increases as the feature space has fewer and fewer dimensions. These simulation results show, however, that our computational diffractive imager design should yield an acceptable single-frame detection error rate of roughly 0.1 with as few as 100 features.

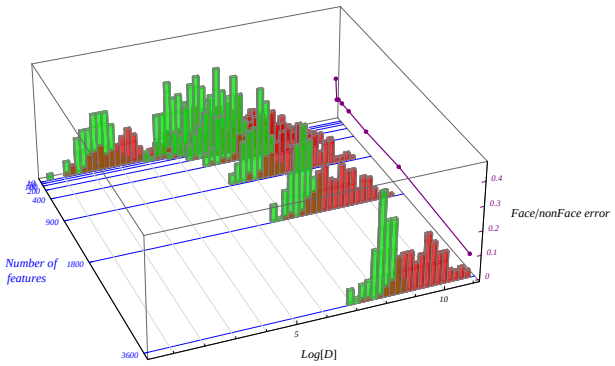

Fig. 11. The performance of a lensless ultra-miniature diffractive sensor for distinguishing faces from non-faces. The logarithm of the distance D in the full 3600-dimensional space and in subspaces of lower dimension (as listed at the left in blue) are shown. Along a blue line marking a given number of features, each green histogram represents the number of face patterns that have the indicated distance to other face patterns and each red histogram represents the (larger, on average) distance from a face to a non-face. The optimal classification rule is based on the crossing point of the red and the green histograms, and the overlap of the histograms represents the relative face/non-face classification error.

VI. Final remarks

We have designed and verified through full end-to-end system simulation a new class of lensless computational imagers based on phase anti-symmetric spiral gratings. We have built the components and are moving towards full hardware characterization of gratings and verification of imaging functionality. These imagers promise to be smaller (lower physical volume) than any existing lens-based imagers of comparable resolution, very inexpensive, and customizable to both imaging and a wide range of sensing and image measurement tasks. A full description of the hardware manufacture, calibration, and imaging performance are presented elsewhere [25].

Practical fielded applications will lead to many interesting problems in efficient application-specific algorithms, either on special-purpose ASICs, on highly parallel graphics processor units (GPUs), or on general-purpose central processor units (CPUs). Networks of such sensors highlight several problems and opportunities in power usage and bandwidth optimization.

Acknowledgments

We thank Thomas Vogelsang and Michael Ching for helpful comments.

References

[1] D. G. Stork and P. R. Gill, "Lensless ultra-miniature computational sensors and imagers," in *SensorComm 2013*, Barcelona, Spain, 2013.

[2] P. R. Gill, C. Lee, D.-G. Lee, A. Wang, and A. Molnar, "A microscale camera using direct Fourier-domain scene capture," *Optics Letters*, vol. 36, no. 15, pp. 2949–2951, 2011.

[3] T. Gustavson, *Camera: A history of photography from Daguerreotype to digital*. New York, NY: Sterling Publishing Co., 2009.

[4] D. Wooters and T. Mulligan, *A history of photography—from 1839 to the present*. New York, NY: Taschen, 2005.

[5] D. Falk, D. Brill, and D. G. Stork, *Seeing the light: Optics in nature, photography, color, vision and holography*. New York, NY: Wiley, 1986.

[6] M. V. Klein, *Optics*. New York, NY: Wiley Publishing, 1970.

[7] D. J. Brady, *Optical imaging and spectroscopy*. New York, NY: Wiley and Optical Society of America, 2009.

[8] T. Vogelsang, D. G. Stork, and M. Guidash, "Hardware validated unified model of multibit temporally and spatially oversampled image sensors with conditional reset," *Journal of Electronic Imaging*, vol. 23, no. 1, p. 013021, 2014.

[9] W. T. Cathey and E. R. Dowski, Jr., "A new paradigm for imaging systems," *Applied Optics*, vol. 42, no. 29, pp. 6080–6092, 2002.

[10] D. G. Stork and M. D. Robinson, "Theoretical foundations of joint design of electro-optical imaging systems," *Applied Optics*, vol. 47, no. 10, pp. B64–75, 2008.

[11] E. H. Adelson and J. Y. A. Wang, "Single lens stereo with a plenoptic camera," *IEEE Transactions on Pattern Analysis and Machine Intelligence*, vol. 14, no. 2, pp. 99–106, 1992.

[12] A. Levin, R. Fergus, F. Durand, and W. T. Freeman, "Image and depth from a conventional camera with a coded aperture," *ACM Transactions on Graphics*, vol. 26, no. 3, pp. 70:1–70:9, 2007.

[13] D. L. Marks, D. S. Kittle, H. S. Son, S. H. Youn, S. D. Feller, J. Kim, D. J. Brady, D. R. Golish, E. M. Vera, M. E. Gehm, R. A. Stack, E. J. Tremblay, and J. E. Ford, "Gigapixel imaging with the AWARE multiscale camera," *Optics and Photonics News*, vol. 23, no. 12, p. 31, 2012.

[14] D. L. Donoho, "Compressed sensing," *IEEE Transactions on Information Theory*, vol. 52, no. 4, pp. 1289–1306, 2006.

[15] M. F. Duarte, M. A. Davenport, D. Takhar, J. N. Laska, T. Sun, K. F. Kelly, and R. G. Baraniuk, "Single-pixel imaging via compressive sampling," *IEEE Signal Processing Magazine*, vol. 25, no. 2, pp. 83–91, 2008.

[16] J. M. Kahn, R. H. Katz, and K. S. J. Pister, "Next century challenges: Mobile networking for 'Smart Dust'," in *Proceedings of the 5th Annual ACM/IEEE International Conference on Mobile Computing and Networking (MobiComm 99)*, 1999, pp. 271–278.

[17] P. R. Gill, C. Lee, S. Sivaramakrishnan, and A. Molnar, "Robustness of planar Fourier capture arrays to colour changes and lost pixels," *Journal of Instrumentation*, vol. 7, pp. C01–61, 2012.

[18] A. Wang and A. Molnar, "A light-field image sensor in 180 nm CMOS," *IEEE Journal of Solid-State Circuits*, vol. 47, no. 1, pp. 257–271, 2012.

[19] A. Wang, P. R. Gill, and A. Molnar, "Light field image sensors based on the Talbot effect," *Applied Optics*, vol. 48, no. 31, pp. 5897–5905, 2009.

[20] S. Sivaramakrishnan, A. Wang, P. R. Gill, and A. Molnar, "Enhanced angle sensitive pixels for light field imaging," in *IEEE International Electron Devices Meeting (IEDM)*, 2011, pp. 8.6.1–8.6.4.

[21] C. Peroz, S. Dhuey, A. Goltsov, M. Volger, B. Harteneck, I. Ivonin, A. Bugrov, S. Cabrini, S. Babin, and V. Yankov, "Digital spectrometer-on-chip fabricated by step and repeat nanoimprint lithography on pre-spin coated films," *Microelectronic Engineering*, vol. 88, no. 8, pp. 2092–2095, 2011.

[22] O. Cossairt, M. Gupta, and S. Nayar, "When does computational imaging improve performance," *IEEE Transactions on Image Processing*, vol. 22, no. 2, pp. 447–458, 2013.

[23] O. Cossairt, M. Gupta, K. Mitra, and A. Veeraraghavan, "Performance bounds for computational imaging," *Imaging and Applied Optics*, 2013.

[24] P. R. Gill and D. G. Stork, "Lensless ultra miniature imagers using odd-symmetry phase gratings," in *Proceedings of Computational Optical Sensing and Imaging (COSI)*, Alexandria, VA, 2013.

[25] ——, "Hardware verification of an ultra-miniature computational diffractive imager," in *Proceedings of Computational Optical Sensing and Imaging (COSI)*, Kohala Coast, HI, 2014.

[26] R. L. Morrison, "Symmetries that simplify the design of spot array phase gratings," *Journal of the Optical Society of America A*, vol. 9, no. 3, pp. 464–471, 1992.

[27] P. R. Gill, "Odd-symmetry phase gratings produce optical nulls uniquely insensitive to wavelength and depth," *Optics Letters*, vol. 38, no. 12, pp. 2074–2076, 2013.

[28] R. Penrose and J. A. Todd, "On best approximate solutions of linear matrix equations," *Mathematical Proceedings of the Cambridge Philosophical Society*, vol. 52, pp. 17–19, 1956.

[29] D. G. Manolakis, V. K. Ingle, and S. M. Kogon, *Statistical and adaptive signal processing: Spectral estimation, signal modeling, adaptive filtering and array processing*. Norwood, MA: Artech, 2005.

[30] T. Hastie, R. Tibshirani, and J. Friedman, *Elements of statistical learning: Data mining, inference, and prediction*. New York, NY: Springer, 2009.

[31] D. A. Fish, A. M. Brinicombe, E. R. Pike, and J. G. Walker, "Blind deconvolution by means of the Richardson-Lucy algorithm," *Journal of the Optical Society of America A*, vol. 12, no. 1, pp. 58–65, 1995.

[32] D. G. Stork, "Joint optics/signal processing design for computational diffractive sensing and imaging," in *Computational Optical Sensing and Imaging (COSI)*, Kohala Coast, HI, 2014.

[33] D. Tseng, O. Mudanyali, C. Oztoprak, S. O. Isikman, I. Sencan, O. Yaglidere, and A. Ozcan, "Lensfree microscopy on a cellphone," *Lab on a chip*, vol. 14, pp. 1787–1792, 2010.

[34] H. Chaouchi, Ed., *The Internet of Things: Connecting objects*. New York, NY: Wiley, 2010.

[35] R. O. Duda, P. E. Hart, and D. G. Stork, *Pattern Classification*, 2nd ed. New York, NY: Wiley, 2001.

[36] D. G. Stork and P. R. Gill, "Reading QR code symbols with an ultra-miniature computational diffractive imager," in *Proceedings of Computational Optical Sensing and Imaging (COSI)*, Kohala Coast, HI, 2014.

[37] S. Z. Li and A. K. Jain, Eds., *Handbook of face recognition*. New York, NY: Springer, 2005.